

13 (T13) using an anemometer. Thermocouple 11 (T11) malfunctioned at the time the test was being performed, however, the deviation between the proportion in respect to T13 and T11 was marginal. Accordingly, the mean and standard deviation corresponding to the difference in proportion, $(p(T-11) - p(T-13))$, is 0.024 and 0.003 for cases 1-5. The relationship between steady-state temperature and wind speed is to be deduced as a function according to the specified environmental conditions and heat load (W-A).

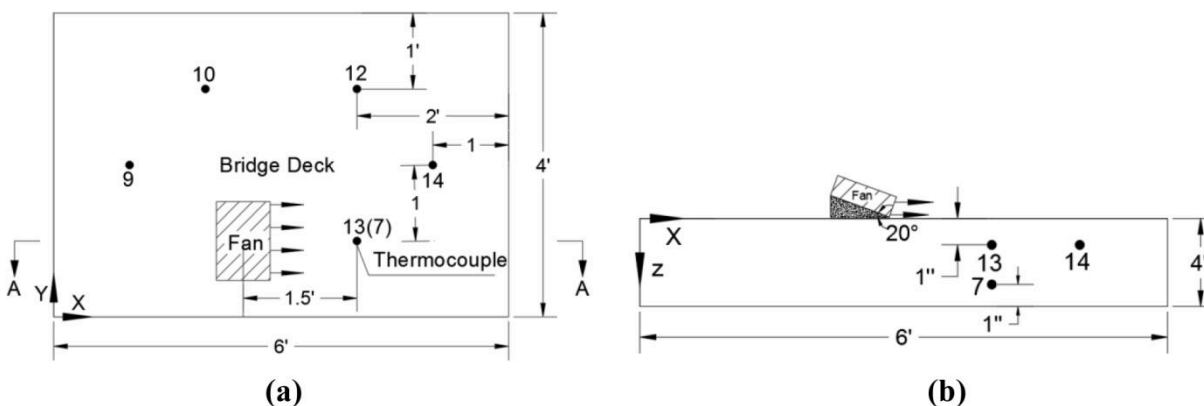


Figure 5. Bridge deck used in wind effect test and set up of thermocouples; a) plane view, b) A-A cross-section view.

Table 1. Steady-state temperatures and proportions

Wind Speed (mph)	Steady-state Temperature (S, °F)	$P = S-A/(W-A)$
0	48.8	0.27
4	43.7	0.114
6.8	42.4	0.078
10.2	42.0	0.066
24	41.0	0.062
28	40.9	0.0613

** Average heat load (W-A) = 34 °F, average ambient (A) = 40 °F **

Test results

Table 1 shows the steady-state temperatures and proportions corresponding to different wind speeds. Figure 6 (a) shows the change in proportion for thermocouple 13 in respect to the following environmental conditions: $W_d = 4$ mph, $A = 55^\circ$ F, $W = 110^\circ$ F. The proportion stabilized around 0.11, which is significant considering that $p_{avg} \sim 0.27$ with no wind present. Therefore, the heating efficiency of the system is compromised extensively due to the wind. Figure 6 (b) shows the change in proportion experienced due to winds set at 28 mph. As shown, the proportion at equilibrium stabilized at 0.061 towards the end of the test.

Figure 7 represents the exponential factor γ , which is interpolated using the change in thermal gradient ratio, p in respect to varying wind speeds. The factor is utilized to solve p for winds in the range of 0 to 40 mph. The last endpoint was extrapolated based on the trend. The following equation can be utilized to solve all proportion inputs (from the table) to equate gamma:

$$p = 0.27 * e^{-(\gamma) * x} \tag{2}$$

Where x denotes the wind speed in mph and 0.27 is the initial average proportion concerning T13 based on multiple tests under different environmental conditions. The exponential factor, γ , was then interpreted as the best-fit equation from the data points exhibited from equation 2. If the wind speed and proportion were chosen as 6.8 mph and 0.077, respectively, the exponential factor γ would be 0.182. Using the best-fit equation for gamma from the plot, $\gamma = 0.167$, which yields a deviation of 8.2% from the experimental value. Accordingly, the equation shown in Figure 6 is appropriate for predicting the proportion, p .

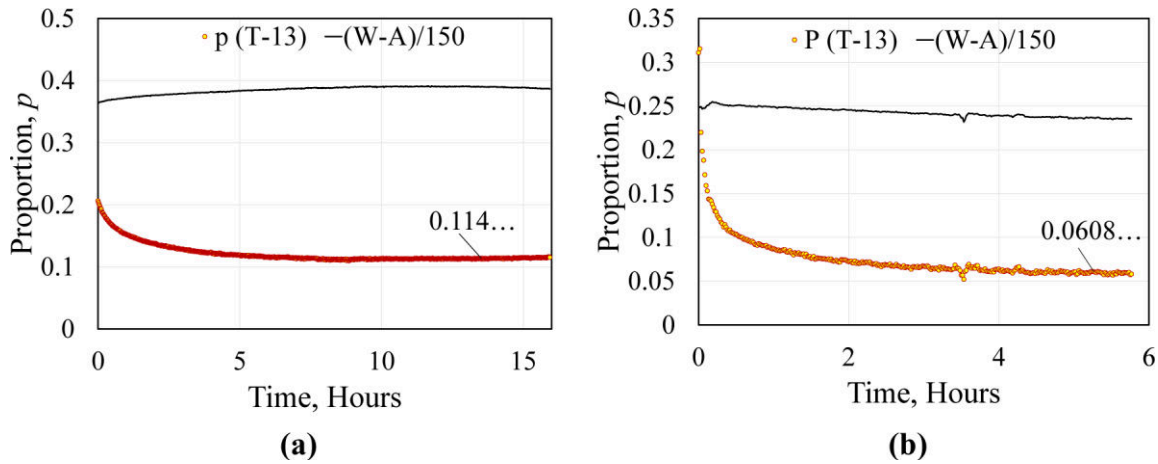


Figure 6. Proportion (Wd = 4mph), (b): Proportion (Wd = 28 mph)

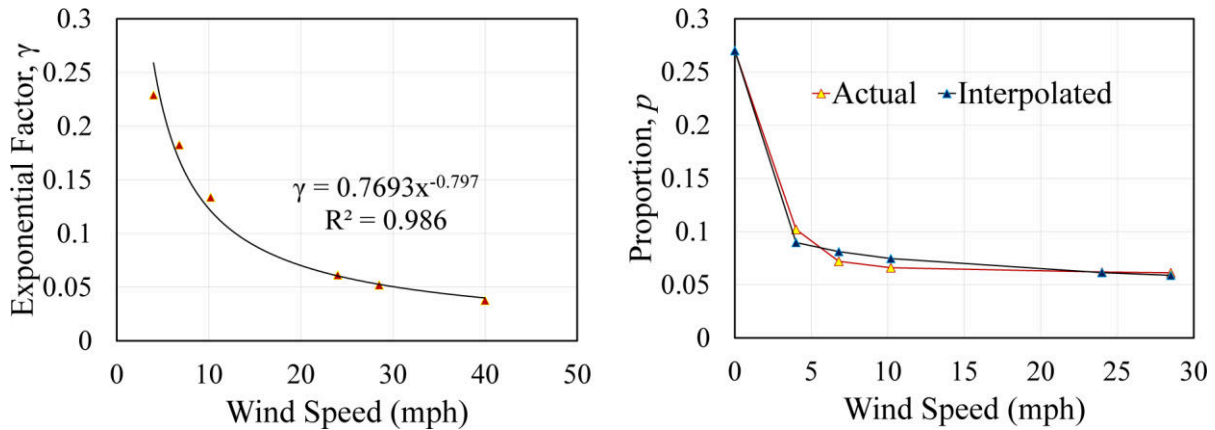


Figure 7. (a): Exponential Factor, γ , (b) Proportion as a Function of Wind Speed

Figure 7 (b) illustrates the major effect of sustained wind on transferring heat away from the surface of the slab. The limit of convergence is roughly 0.05, meaning that the proportion of heat transfer will slightly decrease when the wind speed reaches a certain threshold. It can also be deduced from the trend that heat loss at the surface of the slab follows a negative exponential function. Sustained wind, however, will overestimate the quantity of heat loss relative to actual conditions. Hence, the figures correspond to the worst case scenario, in which wind is continuously fixed. In actuality, the wind will continuously fluctuate and may cease periodically. Thus, there would exist a rebound effect in regards to the proportion, p . Using Figure 7 (a) and letting $x = 28$, the exponential function yields $p = 0.059$, which is only deviated by 3.2 % from the actual experimental value (0.061). Therefore, the exponential function is a good approximation of the proportion, p for sustained winds within a range of 4 to 28 mph. The portion of the curve was assumed linear for wind speeds less than 4 mph.

EFFECT OF WIND ON ALTERED ENVIRONMENTAL CONDITIONS

The objective of this test was to determine the temperatures on plane 2, i.e., 1 inch below the slab top surface, in response to various thermal loads (W-A) and wind conditions (Wd).

Experimental Setup

The dimensions of the bridge deck and the arrangement of the thermocouples are shown in Figure 8. The origin of the coordinate system was located at the left bottom corner of the deck top surface, and Z is upward. Thermocouples were installed to monitor the temperature response inside the slab and the loop. To simulate the effect of wind, a fan with three-speed modes was set near thermocouple 11. The location of the fan and thermocouples are shown in Table 2. Heat generated from fan motor was not considered as negligible in altering the air temperature.

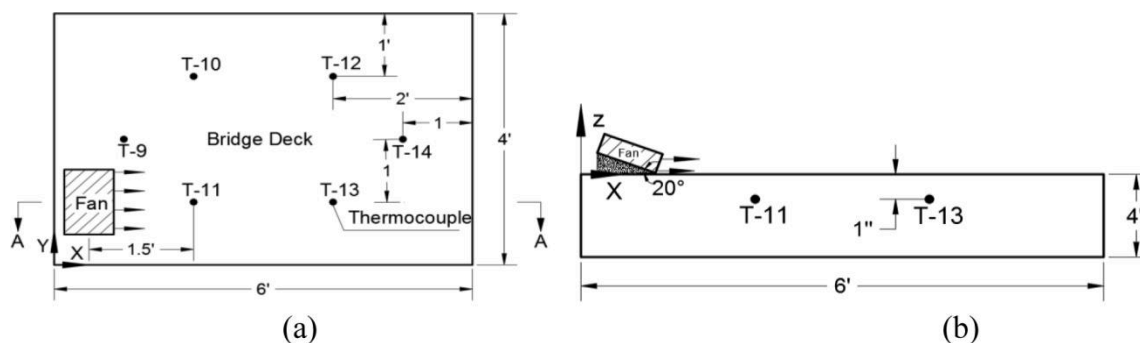


Figure 8. Bridge deck used in wind effect test and set up of thermocouples; a) plane view, b) A-A cross-section view.

Table 2. Location of fan and thermocouples

Thermocouple /Fan Number	Coordinates		
	X (ft.)	Y(ft.)	Z(in.)
Fan (center)	0.5	1	0
T-11	2	1	-1
T-13	4	1	-1

Experimental Conditions and Procedures

A series of four tests were conducted under different thermal loads. Each test series is defined according to the following ambient temperatures: 40, 45, 55, and 62.5° F and contains two sub-tests so that the wind speed was directed over thermocouple 11 at a distance of 3" from the base of the slab. A high-power fan was angled slightly and directed near thermocouple 11 (T11). The wind direction was positioned so that thermocouple 13 (T13) was also in the influence zone. Each sub-test was defined according to wind speed. The fan had three selected power modes: H = high, M = medium, and L = low. For this test, only the power modes of low and high were utilized.

Initially, the fan was directed towards thermocouples 11 at low speed from a distance of 1.5 feet. The fan stayed on low speed for 18-24 hours to ensure that the equilibrium conditions were met. Then, the fan was turned up to high speed. Once equilibrium conditions were met in response to the high wind speed, the test sequence was finished. The next sub-test was initiated after 6-8 hours to allow the temperature to stabilize. Before each test sequence, the initial steady-

state temperature was recorded for the respected thermocouples. Following each sub-test, the final steady-state temperatures were recorded under the influence of wind. The flow rate was 1 gal./min.(0.6m³/s) for all of the tests The wind speed was measured as 24 mph and 30 mph respectively at the location directly above thermocouple 11 when the fan was on low and high-speed mode.

TEST RESULTS AND ANALYSES

The test results corresponding to each test sequence is shown in table 3. The corresponding thermal gradient ratio at initial steady state is defined as p^* . Following each sub-test, the final steady-state temperatures and the final thermal gradient ratios (p^{**}) were recorded as the proportion of the heat load was maintained under the influence of wind. The difference between the two proportions p^* and p^{**} signifies the proportion of heat dissipated from the slab as a function of the rate of convective heat transferred to the environment.

Table 3 presents the mean and standard deviations of p^{**} for each wind mode. It can be observed that the final proportion after wind was introduced (p^{**}) was very consistent, regardless of the environmental circumstances. Further, the variance in the final proportion in respect to the two wind loads was quite small, indicating that a slight change will be seen when wind speed is higher than 30 mph. Figure 9 (a) shows the tabulated results regarding the relationship between thermal load and the proportion, p . The deviation among the values can be attributed to the following:

1. Some of the tests were conducted in a shorter time span and hence may not have achieved equilibrium.
2. The environmental chamber temperature steadily crept up for a few tests. However, the change was marginal (Note: The slight fluctuation in ambient temperature can be observed in table 3 (45-90) as the high fan mode immediately succeeded the low fan mode).

By inputting p^{**} into (1), the steady state temperature of a 4" slab exposed to sustained winds of 24 mph to 30 mph can be estimated with reasonable accuracy.

Figure 9 (b) illustrates the process of thermal dissipation corresponding to variable wind speeds at an ambient temperature of 45°F. The results were compiled from the thermal gradient ratio, p , obtained from the aforementioned tests at different heat loads. Multiple heat loads were applied for wind speeds ranging from 4 to 30 mph. The initial steady-state conditions were obtained from four of the corresponding sixteen cases. The thermal gradient ratio, p , maintained consistency regardless of the heat load. Each line of the phase diagram represents the steady-state conditions at wind speeds, between the data points. For instance, the steady-state temperature for winds sustained at 4 mph would designated by T-11 (wd = 4), and so forth. The minimum data points, denoted as T-11 (wd = 40), represents a hypothetic “worst case” scenario obtained using figure 6. The phase diagram illustrates that the steady state temperature is influenced considerably by wind, and there is not much variation past a certain wind threshold. Accordingly, the wind threshold is estimated around 10 mph, which represents the minimum wind speed at which heat dissipation is no longer a significant factor. It can be observed that the steady state temperature is converging to the ambient temperature (A) quite significantly for wind speeds beyond 4 mph. Further, the negative net change in the steady-state temperature for wind speeds greater than 24 mph is marginal. Lastly, the slope of each line is indirectly proportional to wind speed and hence, the efficiency of the system decreases as a function of wind speed. Therefore, higher heat loads will proportionally contribute less heat as wind speed

increases.

Table 3. Steady-State Temperature of (T-11) Unit (°F)

Test Sequence (A-W-P)	Initial Temp, T-11 (° F)	Final Water Temp. (° F)	Final Ambient Temp. (° F)	Final Temp, T-11 (° F)	p*	p**	p* - p**	\bar{x}	σ
40-60-L	46.3	61.7	39.8	41.6	0.3	0.08	0.22	0.086	0.006
40-70-L	49.1	68.2	40.5	42.8	0.29	0.08	0.21		
40-80-L	51.4	79	40	43.6	0.28	0.09	0.19		
40-60-H	46.3	61.1	40.1	41.5	0.3	0.07	0.23	0.072	0.008
40-70-H	49.1	70	40.1	42.2	0.29	0.07	0.22		
40-80-H	51.4	80.8	40.1	43.4	0.28	0.08	0.2		
45-70-L	52.3	73.1	45.4	47.3	0.3	0.07	0.23	0.075	0.004
45-80-L	55.9	81.5	45.1	47.9	0.31	0.08	0.23		
45-90-L	57.2	89.3	45.5	48.8	0.27	0.07	0.2		
45-100-L	60	99.1	47.3	51.3	0.27	0.07	0.2	0.063	0.002
45-70-H	52.3	72.4	45.6	47.2	0.3	0.06	0.24		
45-80-H	55.9	81.8	44.9	47.3	0.31	0.07	0.24		
45-90-H	57.2	89.4	46.7	49.4	0.27	0.06	0.21		
45-100-H	60	99.8	47.7	51	0.27	0.06	0.21		

Sustained wind speeds at power level: Low ~ 24 mph, high ~ 30 mph

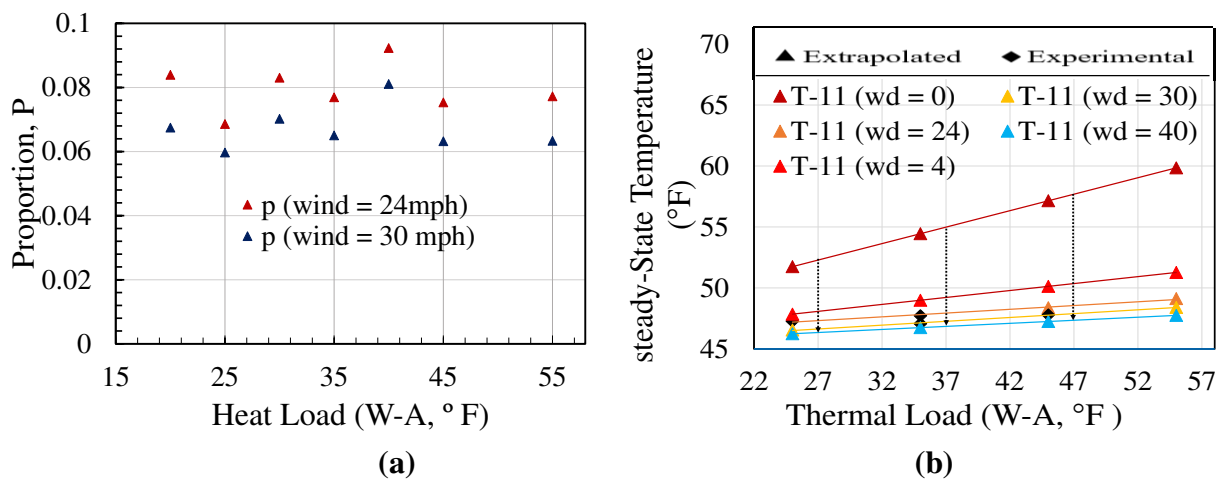


Figure 9. (a): Range in Proportion for Low and High Wind Speeds, (b) Phase Diagram Relating Steady-State Temperature as a Function of Wind Speed

CONCLUSIONS

Heating tests of an externally heated hydronic slab were performed inside an environmental chamber under various room temperatures, water temperatures, and wind speeds. The steady-state temperature at 1 inch below the top surface was observed to be linearly proportional to the heat load (W-A) for multiple cases. Test results corresponding to the influence of sustained wind projected at the slab were analyzed. The test analyses results show that wind significantly increases the amount of heat loss from the slab. Wind dramatically reduces the efficiency of heating as a consequence of convection heat loss. This effect can be directly observed by a decrease in the rate of change corresponding to the steady-state temperatures for increased wind speeds. Further, the heating efficiency is quite sensitive for low wind speeds (Wd <10 mph). More testing needs to be performed at various sub-freezing conditions to determine the net negative effect of each environmental factor on the thermal gradient ratio, *p*.

REFERENCES

- Bowers, G. A., and Olgun, C. G. (2015). "Experimental Investigation of Bridge Deck Deicing Using Energy Piles." *IFCEE 2015*, M. Iskander, M. T. Suleiman, J. B. Anderson, and Debra F. Laefer, eds.
- Bowers Jr, G., and Olgun, C. "Ground-Source Bridge Deck Deicing Systems Using Energy Foundations." *Proc., Geo-Congress 2014 Technical Papers@ Geo-characterization and Modeling for Sustainability*, ASCE, 2705-2714.
- Ceylan, H. (2014). "PEGASAS FAA COE Project No. 1: Heated Airport Pavements."
- Eugster, J. "Road and Bridge Heating. Using Geothermal Energy. Overview and Examples." *Proc., Proceedings European Geothermal Congress*.
- Griffin, R. G. (1982). "Highway Bridge Deicing Using Passive Heat Sources." *Publication No. FHWA-CO-82-7, Colorado Dept. of Highways. Springfield, VA*.
- Li, T., Lei, G., Yu, X., Zhang, N., and Puppala, A. J. "Numerical Feasibility Study of an Externally Heated Geothermal Bridge Deck." *Proc., IFCEE 2018*.
- Lund, J. W. (2000). "Pavement snow melting." *Geo-Heat Center Quarterly Bulletin*, 21(2), 12-19.
- Minsk, L. D. (1999). "Heated bridge technology: report on ISTE A Sec. 6005 program."
- Swanson, H. N. (1980). "Evaluation of Geothermal Energy for Heating Highway Structures." Colorado Department of Highways.
- Tobar, D. P. E. (2003). *Experimental and Computational Investigation of Snow Melting on a Hydronically Heated Concrete Slab*, Oklahoma State University.
- Xinbao Yu, Mark Timothy Hurley, Teng Li, Aravind Pedarla, Anand J. Puppala. Laboratory Evaluation of an Attached Hydronic Loop Design for Geothermal Heated Bridge Deck. *Journal of Cold Regions Engineering*.
- Wadivkar, O. (1997). "An Experimental And Numerical Study Of The Thermal Performance Of A Bridge Deck De-Icing System." Master of Science Thesis, Oklahoma State University, Stillwater, OK.

Using Soil-Moisture Active Passive Satellite Data to Evaluate the Performance of Transportation Infrastructure Foundations—A Feasibility Study

Simon Packman¹; Sonya Lopez, Ph.D.²; Aria Fathi, S.M.ASCE³;
and Mehran Mazari, Ph.D., A.M.ASCE⁴

¹California State Univ. Los Angeles, Dept. of Civil Engineering and NASA Data Intensive Research and Education Center for STEM, 5151 University Dr., Los Angeles, CA 90032. E-mail: spackma@calstatela.edu

²California State Univ. Los Angeles, Dept. of Civil Engineering and NASA Data Intensive Research and Education Center for STEM, 5151 University Dr., Los Angeles, CA 90032. E-mail: slope188@calstatela.edu

³Center for Transportation Infrastructure Systems (CTIS), Univ. of Texas at El Paso, 500 W. University Ave., El Paso, TX 79968. E-mail: afathi@miners.utep.edu

⁴California State Univ. Los Angeles, Dept. of Civil Engineering, 5151 University Dr., Los Angeles, CA 90032. E-mail: mmazari2@calstatela.edu

ABSTRACT

NASA's soil moisture active passive (SMAP) satellite measures the near-surface soil moisture (0–5 cm depth) everywhere on Earth's surface. It produces global soil moisture maps [in m^3/m^3] at the 9 km spatial and 24-hour temporal resolution. SMAP launched in January 2015 and has been collecting observations for a three-year period (2015–2018), with a 2–3 day temporal resolution. SMAP's global soil moisture maps can be used to improve weather forecasts, increase our understanding of the water and carbon cycle, monitor droughts, and predict timing and location of floods. The radar observations could be superimposed on a map of transportation infrastructures to evaluate their performance under excessive water intrusion. This study included a analysis to evaluate the moisture-induced performance of transportation infrastructure foundations and pavement layers. The SMAP data were extracted within the study area before and during a major weather event. Other remote sensing products that monitor precipitation and groundwater changes were also employed to determine the level of infrastructure inundation. The results of this evaluation process suggest the feasibility of using SMAP data to investigate the performance of transportation infrastructure foundation layers under inundated conditions.

INTRODUCTION

One of the most important components of our transportation infrastructure is the road network. Pavement structures are the main elements of road assets that need to be maintained, rehabilitated and reconstructed. The performance of pavement structure is significantly affected by environmental factors such as extreme hot and cold temperatures, and water intrusion above and below the pavement resulting from heavy precipitation events. Performance assessment of pavements is thus of major interest to highway agencies and stakeholders in coastal regions during extreme weather events.

The road pavement system is in continuous interaction with its environment. Different environmental factors are being considered while designing pavement systems. The Mechanistic Empirical Pavement Design Guide (MEPDG) incorporates the environmental factors as an Enhanced Integrated Climate Model (EICM). The EICM simulates the impact of environmental

conditions on pavement characteristics and properties. Initial EICM was developed by Federal Highway Administration (FHWA) and later was implemented in the pavement design guide (Witczak et al, 2004). One of the major components of environmental impacts of pavement structures is the moisture variation in terms of either precipitation or flooding during a storm surge or other extreme weather events. The primary reason to study the moisture variation in pavement systems is the effect of moisture on strength of geomaterial layers in terms of resilient modulus (MR) and stiffness. Increased moisture content in compacted geomaterial layers result in declining strength as the water fill in the voids in materials and decrease the interlocking of soil particles (Sotelo et al. 2014, Mazari et al. 2015, Nazarian et al. 2015). An excessive amount of water in pavement structure may result in a reduction of structural performance and loss of load bearing capacity of the pavement system. This scenario is more likely to happen during or after extreme events such as flash floods, sea level rise and storm surges. Evaluating the short- and long-term structural capacity of pavement structure during and after weather events is of particular interest for decision makers when assessing the resilience of transportation infrastructures.

Water may enter the pavement system from above due to inundation and below due to capillary rise within the subsurface soil layers. Extreme weather events could vastly contribute to the damage proneness of pavement layers, and more specifically foundation soil layers. This was observed by the Louisiana Department of Transportation due to Hurricane Katrina (Zhang et al., 2008). The International Panel of Climate Change (IPCC) projects a sea-level rise of about 60 cm due to melting of the ice caps (IPCC, 2007). This projection indicates that pavement systems in coastal areas can be fully inundated due to high tides and sea level rise. Structural performance and load bearing capacity of the pavement system are affected by the reduced strength of subgrade soil due to the presence of water. However, these effects are not visible and may lead to the failure of road infrastructure under traffic loads. Evaluating the structural performance of pavements under flooded conditions could help to prevent the structural failure.

The evaluation of post-event condition of roadways and flooded transportation infrastructure have been limited to few recent studies such as hurricane Katrina in Louisiana (Chen and Zhang, 2011) and hurricane Sandy in New York and New Jersey (Kaufman et al, 2012). The impact of such events is even more visible on low-volume and gravel roads. The local highway agencies need a decision support system to evaluate the performance of affected infrastructure and decide for remedial and repair strategies.

The scope of this paper is to utilize remote sensing data to estimate moisture levels in the pavement infrastructures and strength of the roads. It is noteworthy that FHWA initiated an international effort to address the vulnerability of roadway structure after flooding (FHWA, 2012). The scope of this paper aligns with the FHWA Flooded Pavement Assessment and considers the following objectives (FHWA, 2012):

- Identify when emergency or other vehicles can safely be allowed on roads of different types, and on different soils, that have been or are flooded to various degrees (i.e. depths and durations).
- Determine the best times to allow heavy maintenance equipment on the roads (e.g. in terms of the tradeoff between the user costs of road closure versus costs of increased road damage).
- Determine the effects of floods on long-term pavement performance.
- Develop guidelines for use by highway agencies on how to assess flooded pavements for both short term and long-term impacts.

That research was planned to be performed in two phases. Phase I included an extensive review of methods, equipment, and instrumentation that could be used to evaluate the short- and long-term structural capacity of flooded pavements. The outcomes of Phase I were implemented in the work plan for Phase II of the study to propose the procedures, methods, and algorithms to evaluate the conditions of pavement structures under flooding and inundation events. The analytical procedures and the decision support system developed as a part of FHWA study could help the coastal communities to predict the optimum time to resume the transportation infrastructure operation (FHWA, 2012).

Satellite data and remote sensing products have served as a valuable source of information regarding the condition of surface earth layers at several spatial and temporal resolutions since the 1970's (Schowengerdt, 2006). Combining these sources of data with the knowledge of pavement structural performance under various environmental conditions could be an alternative methodology in evaluating the resilience of transportation infrastructure network. The following sections include more details regarding the impact of moisture variation on the strength of pavement foundation layers and the integration of satellite data in that evaluation process.

METHODOLOGY

According to the Mechanistic-Empirical Pavement Design Guide (MEPDG), the effects of the environmental factors on the Resilient Modulus (MR) of pavement structures can be evaluated using an environmental factor as follows:

$$MR = F_{env} \times MR_{opt} \quad (1)$$

where F_{env} is the composite environmental adjustment factor and MR_{opt} is the resilient modulus at optimum conditions and at any stress level. Witczak et al. (2000), as part of the development of the MEPDG, proposed the following equation:

$$\log(F_{env}) = \log\left(\frac{M_R}{M_{Ropt}}\right) = a + \frac{b-a}{1 + e^{\left(\frac{\ln(-b+a+k_m \times (S-S_{opt}))}{a}\right)}} \quad (2)$$

where MR = modulus at a degree of saturation S ; MR_{opt} = modulus at the maximum dry density and optimum moisture content; S_{opt} = degree of saturation (in decimal) at the maximum dry density and optimum moisture content; a = minimum of $\log(MR/MR_{opt})$ (-0.3123 and -0.5934 for coarse- and fine-grained materials, respectively); b = maximum of $\log(MR/MR_{opt})$ (0.3010 and 0.3979 for coarse- and fine-grained materials, respectively); k_m = regression parameter (6.8157 and 6.1324 for coarse- and fine-grained materials, respectively). Cary and Zapata (2010) further studied the impact of moisture variation and proposed a more specific form of Eq. 2 by incorporating additional geomaterial properties including the percent finer than No. 200 sieve (w , in decimals) and plasticity index of the geomaterials (PI , in percent) as follows:

$$\log(F_{env}) = (\alpha + \beta \times e^{-wPI})^{-1} + \frac{(\delta + \gamma \times wPI^{0.5}) - (\alpha + \beta \times e^{-wPI})^{-1}}{1 + e^{\left(\frac{\ln\left(\frac{-(\delta + \gamma \times wPI^{0.5})}{(\alpha + \beta \times e^{-wPI})^{-1}}\right) + (\rho + \omega \times e^{-wPI})^{0.5} \times \left(\frac{S-S_{opt}}{100}\right)}\right)}} \quad (3)$$

where $\alpha = -0.600$, $\beta = -1.87194$, $\delta = 0.800$, $\gamma = 0.080$, $\rho = 11.96518$, and $\omega = -10.19111$. Their equation appears to be empirical and requires the determination of resilient moduli at optimum conditions. Toward development of modulus-moisture equations, some other studies such as Oh and Fernando (2011), Siekmeier (2011) and Mohammad et al (2002) reported the modulus as a function of soil suction, moisture level, and stress conditions. Those equations are based on the

MEPDG guidelines and account for principles of unsaturated soil mechanics.

In order to further simplify Eq. 3, Nazarian et al. (2015) suggested that assuming a $wPI=0$ in Eq. 3 could represent a wide range of geomaterials. Replacing all other constants in Eq. 3, the following equation could be employed in estimating the environmental factor:

$$\log F_{env} = \left[(-0.40535) + \frac{1.20693}{1 + e^{\left[0.68184 + 1.33194 \times \left(\frac{S - S_{opt}}{100} \right) \right]}} \right] \quad (4)$$

The degree of saturation (S) can be estimated using the following equation:

$$S = G_s \frac{\omega}{e} \quad (5)$$

where S is degree of saturation, G_s is specific gravity, ω is volumetric moisture content, and e is void ratio. The following sections include a discussion of extracting soil moisture (ω) during a major extreme event using large-scale satellite data and exploring the feasibility of applying those environmental factors to evaluate the strength of road foundation layers.

Remote Sensing Products

Four remote sensing products were used in the hydrologic analysis of this study to obtain estimates of near-surface soil moisture, water table depth, precipitation, and surface inundation during the period of analysis. Near-surface soil moisture estimates (0-5 cm depth) were obtained using NASA's Soil Moisture Active Passive (SMAP) measurements (Panciera et al., 2014). The SMAP satellite was launched in January 2015 and produces global volumetric soil moisture maps [in cm^3/cm^3] with an unbiased root mean squared error no greater than $0.04 \text{ cm}^3/\text{cm}^3$ (Kerr et al., 2010; Entekhabi et al., 2014). This work used the SMAP Level-3 daily global product at a 9 km spatial resolution.

NASA's Gravity Recovery and Climate Experiment (GRACE) was used to estimate water table depth. The GRACE product provides groundwater storage in percentage of storage filled, for which 100 percent storage indicates the subsurface storage is filled. GRACE has been previously used to assess regional flood potential (Reager et al., 2015) and model flood inundation (Lucey et al., 2017). The GRACE satellite takes measurements at a 0.125-degree spatial resolution on a 7-day time interval. The GRACE sensor also provides an estimate of percent soil moisture or percent of subsurface pore-space filled with water within the top 5 cm. GRACE observations in this study were extracted for the period of July 31, 2017, to August 28, 2017, which was the same period that hurricane Harvey struck the coast of Texas in the United States.

The hourly North American Land Data Assimilation Product (NLDAS-2) was used to estimate total precipitation during the study period. NLDAS-2 is a gridded product that uses Stage II/IV gauge observations of hourly precipitation forcing to derive a 1/8 degree. To aggregate to daily precipitation total (from mmhr^{-1}), total hourly precipitation was used. Kwak et al. (2014) developed a technique to determine flood risk and inundation using Moderate Resolution Imaging Spectrometer (MODIS), and a digital elevation model. This method is considered a feasible approach for detection of instant inundation. Various MODIS daily optical images at a spatial resolution, depending on the wavelength band, including 250, 500, and 1000 m. Surface inundation and flood risk can be calibrated using observations provided by National Oceanic and Atmospheric Administration's National Weather Service River Observations and Forecast database (NOAA-NWS).